Temporal consistency of lidar observables during aerosol transport events in the framework of the ChArMEx/ADRIMED campaign at Menorca Island in June 2013

P. Chazette[1], J. Totems[1], G. Ancellet[2], J. Pelon[2] and M. Sicard[3]

[1]LSCE, CEA-CNRS-UVSQ, UMR 8212, Gif-sur-Yvette, France

[2]Sorbonne Universités, UPMC Université Paris 06, CNRS-UVSQ, UMR 8190 LATMOS, Paris, France

[3]RSLab/IEEC-CRAE, Universitat Politècnica de Catalunya, Barcelona, Spain

Abstract.

We performed synergetic daytime and nighttime active and passive remote sensing observations at Menorca (Balearic Island, Spain), over more than 3 weeks during the Chemistry-Aerosol Mediterranean Experiment / Aerosol Direct Radiative Effect in the Mediterranean (ChArMEx/ADRIMED) special observation period (SOP 1a, June-July 2013). We characterized the aerosol optical properties and type in the low and middle troposphere using an automated procedure combining Rayleigh-Mie-Raman lidar (355, 387 and 407 nm) with depolarization (355 nm) and AERONET Cimel® sun-photometer data. Results show a high variability due to varying dynamical forcing. The mean column-averaged lidar backscatter-to-extinction ratio (BER) was close to 0.024 sr^{-1} (lidar ratio of ~41.7 sr), with a large dispersion of ±33% over the whole observation period due to changing atmospheric transport regimes and aerosol sources. The ground-based remote sensing measurements, coupled with satellite observations, allowed to document i) dust particles up to 5 km (above sea level) in altitude originating from Morocco and Algeria from 15 to 18 June with a peak in aerosol optical thickness (AOT) of 0.25±0.05 at 355 nm, ii) a long-range transport of biomass burning aerosol (AOT = 0.18±0.16) related to North American forest fires detected from 26 to 28 June, 2013 by the lidar between 2 and 7 km and iii) mixture of local sources including marine aerosol particles and pollution from Spain. During the biomass burning event, the high value of the particle depolarization ratio (8-14%) may imply the presence of dust-like particles mixed with the biomass burning aerosols in the mid troposphere. For the field

campaign period, we also show linearity with SEVIRI retrievals of the aerosol optical thickness despite 35% relative bias, which is discussed as a function of aerosol type.

1. Introduction

The Mediterranean has been identified as one of the "hot-spots" in projections of future climate change (Giorgi and Lionello, 2008) and it has been recently shown that aerosol direct and semi-direct effects, which were not properly taken into account in global climate change simulations (IPCC, 2014), have a significant impact on surface temperature, evaporation, and precipitation at the regional scale (Nabat et al., 2015), i.e. a likely positive feedback on the trend for future dryer and thus more turbid Mediterranean summers. Due to the variability of aerosol properties over the Mediterranean basin, this calls for a more representative description of aerosol optical properties and spatiotemporal distribution by both observations and models.

Regional experiments including measurements of the vertical distribution of aerosols were performed some time ago to characterize aerosols over the Mediterranean Sea (i) in the framework of the MEditerranean DUSt Experiment (MEDUSE) in 1997 (Hamonou et al., 1999), (ii) the Scientific Training and Access to Aircraft for Atmospheric Research Throughout Europe (STAAARTE) airborne flights in 1997 (Dulac and Chazette, 2003) and 1998 (Formenti et al., 2002), (iii) with a lidar deployed in Crete (Gobbi et al., 2000) or an instrumented ultralight aircraft in Lampedusa (Di Iorio et al., 2003) during the Photochemical Activity and Ultraviolet Radiation (PAUR II) campaign in 1999, (iv) over the eastern Mediterranean basin during the Mediterranean Intensive Oxidant Study (MINOS; Lelieveld et al., 2002;) and Mediterranean Israeli Dust Experiment (MEIDEX; Levin et al., 2005) in 2001; and (v) over the urban and industrial region of Marseille-Fos-Berre on the French Mediterranean coast also in 2001 (Cros et al., 2004; Cachier et al., 2005) ; (vi) in the framework of the EARLINET network (Papayannis et al., 2008). Such past experiments have

produced very useful information about the vertical distribution of Mediterranean aerosol optical properties, based on in-situ observations and lidar measurements. During those preceding campaigns in the Mediterranean region, the use of aerosol lidars was focused on rather short time periods, but they appear as a very powerful tool to identify the wide spectrum of aerosol types encountered in the tropospheric column (e.g. Chazette, 2003; Chazette et al., 2005a; Berthier et al., 2006; Groß et al., 2011; Tesche et al., 2011; Nisantzi et al., 2014). The multidisciplinary programme Mediterranean Integrated Studies at the Regional and Local Scales (MISTRALS; http://www.mistrals-home.org), initiated by CNRS/INSU in 2010 to study the future habitability of the Mediterranean region, offered the opportunity, within the Chemistry-Aerosol Mediterranean Experiment (ChArMEx, http://charmex.lsce.ipsl.fr), to conduct ground-based and airborne lidar observations at the scale of the Western Mediterranean basin.

The ChArMEx/Aerosol Direct Radiative Effect in the Mediterranean (ADRIMED) special observation period (SOP-1a) was set-up from 11 June to 3 July to study aerosol optical properties and radiative effects in the western Mediterranean during the dry season, which shows a maximum in aerosol optical depth (Nabat et al., 2013). The campaign involved several surface stations throughout the western Mediterranean, research aircrafts, and instrumented balloons (Mallet et al., 2015). In this work, we focus on both active and passive remote sensing observations performed at Menorca (Balearic Island, Spain) during this campaign. The main goal of the paper is to demonstrate the benefit of continuous daytime and nighttime lidar measurements during at least 3 weeks to derive aerosol optical properties. It improves both the assessment of the diurnal variation of the aerosol distribution related to the planetary boundary layer (PBL) growth and the probability to detect long range transports of aerosol plumes. In section 2, we first present the experimental set-up. Retrieved aerosol optical properties for both nighttime and daytime conditions are analysed in section 3 to give

77 an overall identification of aerosol types. In section 4, we discuss the different origins of
78 aerosol particles before discussing comparison with the Spinning Enhanced Visible and
79 InfraRed Imager (SEVIRI) retrievals and concluding in section 5.

80 **2. Ground-based remote sensing measurements**

81 During the campaign, our custom-made Raman lidar WALI (Chazette et al., 2014) was
82 operated together with an AERONET sunphotometer at Cap d'en Font
83 (http://aeronet.gsfc.nasa.gov/new_web/photo_db/Cap_d_En_Font.html) on the south-eastern
84 coast of the Balearic island of Menorca, Spain. The instruments were located within ~6 m
85 from each other, at 39°49'32.9"N, 04°12'29.3"E, at ~10 m above the mean sea level (amsl)
86 and less than 70 m from a small cliff on the sea shore. The choice to use only remote sensing
87 instruments is driven by the lack of representativeness of the ground-based in situ
88 measurements, which are mainly affected by local dynamical forcings. This is especially true
89 in coastal regions (Chazette, 2003). The selected location is mainly affected by Saharan and
90 Spanish air masses. Figure 1 shows the location of the station approximately in the centre of
91 the western Mediterranean basin. The campaign average aerosol optical thickness (AOT_{550}, at
92 550 nm) distribution derived from SEVIRI on-board the geostationary Meteosat Second
93 Generation (MSG) platform is reported in this figure. It shows a classical North-South
94 decreasing gradient in the western Mediterranean Basin due to African dust with maximum
95 values between 0.20 and 0.25 in the Alboran Sea, and minimum values of ~0.12 in the Gulf of
96 Lyon. Intermediate values of ~0.17 are found around Menorca.

97 2.1. Raman lidar

98 The WALI instrument uses an emitted wavelength of 354.7 nm and is designed to fulfil
99 eye-safety conditions. The instrument, its calibration and the associated errors are documented
100 in Chazette et al. (2014) and will not be detailed here. During all the experiment, the
101 acquisition was performed continuously with a vertical resolution of 15 m for mean profiles

of 1000 laser shots leading to a temporal sampling close to 1 min. The presence of clouds was visually detected in the lidar time series of range-corrected lidar backscattered profile and the corresponding periods were removed. Two validated (e.g. Dieudonné et al., 2015) measurement synergy types have been used to retrieve the aerosol optical properties from the lidar. During daytime the sunphotometer AOT_{355} is considered as a constraint for the lidar inversion as in Chazette (2003). Note that using the total AOT only allows us to retrieve a column-averaged or equivalent backscatter-to-extinction ratio (BER, product of the backscatter phase function and the single scattering albedo, inverse of the lidar ratio LR), integrating all the aerosol layers. During nighttime, the two elastic and the N_2-Raman channels of the lidar are used to determine simultaneously the aerosol BER, the vertical profile of the aerosol extinction coefficient (α_e), and the linear particle depolarization ratio (PDR). All methodological details are well presented in Royer et al. (2011), Chazette et al. (2012a) and Chazette et al. (2014). The relative uncertainty on the BER is ~5% (resp. ~10%) during nighttime (resp. daytime). The relative uncertainties on the PDR are close to 10% for the encountered AOT at 355 nm ($AOT_{355} > 0.2$). The relative uncertainty on the AOT is less than 2%. The relative uncertainty on the water vapour mixing ratio (WVMR) is between 7 and 11% within the first kilometres of the atmosphere.

Two representative examples of AOT and BER retrieval are given in Figure 2 corresponding to the main aerosol sources, biomass burning and desert dust observed during this campaign. They demonstrate the good agreement between the cumulative AOT derived from the N_2-Raman and the elastic channels. The calculations have been performed using the average profile of nighttime measurements during the nights of 16-17 and 27-28 June, for biomass and dust cases, respectively. To improve the inversion, the mean profiles have been inverted using an altitude-variable BER and a regularization approach (Royer et al., 2011). For the first example, the BER (LR) is close to 0.04 sr^{-1} (25 sr) in the marine boundary layer (MBL) and

decreases with the altitude to reach values between 0.02 and 0.025 sr^{-1} (50 and 40 sr) between 2 and 3 km amsl. The values of *BER* are similar for the second example in the MBL, but after decreasing below 0.02 sr^{-1} in the aerosol layer above the MBL, they significantly increase above 4 km amsl to reach ~0.025 sr^{-1}. These two profiles correspond to the main contributions of aerosol sources encountered during this period: maritime aerosol in the MBL (BER ~ 0.04 sr^{-1} or LR ~ 25 sr), dust (BER ~ 0.025 sr^{-1} or LR ~ 40 sr) and biomass burning or local pollution (BER < 0.02 sr^{-1} or LR > 50 sr).

2.2. Sunphotometer

The Cimel® sunphotometer is part of the Aerosol Robotic Network (AERONET; http://aeronet.gsfc.nasa.gov/cgi-bin/type_piece_of_map_opera_v2_new; Holben et al., 1998). It performs measurements of solar light extinction at 8 wavelengths in the solar spectrum between 340 and 1020 nm to retrieve the AOT at 7 wavelengths. The instrument field of view is about 1° and the channel bandwidths are less than 20 nm. The instrument was calibrated prior to and after the campaign by the observation service Photométrie pour le Traitement Opérationnel de Normalisation Satellitaire (PHOTONS; http://loaphotons.univ-lille1.fr/), the French component of AERONET. We have used Level-2 quality assured data. The AOT is retrieved with a maximal absolute uncertainty of 0.02, independent of the aerosol load. The aerosol optical thickness at the lidar wavelength of 355 nm (AOT_{355}) has been assessed using the Ångström exponent (Ångström, 1964) and the sunphotometer AOT at 380 and 440 nm. Sunphotometer AOT values at 500 and 675 nm are also used in this work for a better comparison to satellite products described below. Additionally, these measurements were checked against and completed by a SOLAR Light® Microtops II manual sunphotometer, calibrated by PHOTONS shortly before the campaign (AERONET instrument #695). The AOT accuracy is similar to that of the automated Cimel sunphotometer. Nevertheless, manual

151 solar targetting induces an additional bias which leads to an absolute uncertainty of the order
152 of 0.04 as compared to simultaneous measurements by an automated sunphotometer.

153 **3. Temporal continuity of the aerosol optical properties**

154 3.1. Vertically integrated aerosol optical properties derived from the sunphotometer

155 Both times series of AOT at 500 nm (AOT_{500}) and Ångström exponent between 440 and
156 675 nm, as directly measured by the sunphotometer, are plotted in Figure 3.

157 AOT and Ångström exponent both exhibit a strong variability due to the succession of aerosol
158 events of different types, as revealed by the large range of variation of the Ångström exponent
159 between ~0.4 and 2.15. The fine mode fraction of AOT also reported in the figure clearly co-
160 varies with the Ångström exponent. The coarse mode contribution is dominant from 16 to 20
161 June (coarse mode fraction of AOT between 50 and 80%) and also important on 24-25 June
162 (35 to 70%). The AOT appears to be higher with values larger than 0.2 during such periods.
163 The AOT, which is below 0.38 (on 18 June) during the first 2 weeks of campaign,
164 significantly increases on 26-28 June, showing several maxima (up to more than 0.6 on 27
165 June). Variations with particularly large amplitude appear on the 26 and 27 June. Usually
166 such peaks are due to North-African dust aerosol transport over the Western Mediterranean
167 basin (e.g. Moulin et al., 1998; Hamonou et al., 1999). In our case, the Ångström exponent
168 ranging between 1 and 1.6 appears too high to support the hypothesis a dominant presence of
169 dust particles. Values of the Ångström exponent over 1.5 are typical of pollution-like or
170 biomass burning aerosols (Chazette et al., 2005b) and an average value of 1.80 has been
171 observed for non-dust conditions over the Mediterranean by Paronis et al. (1998).
172 Computations by Hamonou et al. (1999) suggest that a dust contribution to this AOT cannot
173 be excluded but should be under a 0.45 fraction for the observed range of Ångström exponent.
174 The lowest AOT values observed on 10 June together with a low range of Ångström exponent
175 (0.01-0.21) are typical of a clear marine atmosphere with an aerosol population dominated by

176 sea-salt particles. We notice that the uncertainty on the Ångström exponent grows as the AOT
177 decreases. For AOT <0.15, the meaning of the Ångström exponent is subject to caution.

178 3.2. Aerosol optical properties derived from the ground-based lidar WALI

179 The temporal evolution of the BER derived from both the lidar measurements and the
180 sunphotometer are compared in Figure 4. The sunphotometer-derived column-integrated BER
181 of the aerosols can be computed from the single scattering albedo and the phase function at a
182 scattering angle of 180° and 440 nm wavelength derived from the operational algorithm of
183 AERONET (Dubovik and King, 2000). The root mean square error (rmse in gray area) on the
184 lidar-derived BER, determined as the variability over 20 minutes, is close to 0.004 sr^{-1} on
185 average, which is comparable with the one retrieved by Chazette et al. (2012b) with a similar
186 lidar system set-up in Menorca in the 2012 autumn season. We note a good coherence with
187 the BER at 440 nm derived by the AERONET sunphotometer. Yet, the sunphotometer-
188 derived BER seems to be underestimated by ~0.004 sr^{-1} to 0.01 sr^{-1} comparatively with the
189 lidar between 19 and 26 June; the larger variability bars at this period are due to a lighter
190 aerosol load (see Figure 3), which may explain part of this discrepancy. The higher values of
191 BER seen by the lidar would also be consistent with the hygroscopic properties of aerosols
192 within the PBL where the relative humidity significantly increases (Figure 4b) to reach more
193 than 90%. Indeed, BER may increase with the growth of aerosols. Moreover, the surface wind
194 speed rose on 26 June, with gusts reaching 12 m s^{-1}, which may seed the atmosphere with
195 marine aerosols (Blanchard et al., 1984).

196 For the sake of checking the consistency between the inversion procedures used during
197 nighttime and daytime, the histograms of the equivalent BER are compared in Figure 5 for
198 daytime, nighttime, and the whole day. These histograms account for all lidar data inverted in
199 cloud-free conditions. The values greater than 0.045 sr^{-1} are not significant and may represent
200 situations where the inversion process does not converge. Hence, ~10% of lidar profiles have

not been considered in the synthesis. The nighttime BER distribution, with a BER value of $0.024\pm0.008\ sr^{-1}$, is only slightly smaller than the daytime distribution ($0.026\pm0.007\ sr^{-1}$). Hence, the BER values are deemed consistent between daytime and nighttime, and the synthesis on the entire experiment period shows an average of $0.024\pm0.008\ sr^{-1}$.

The temporal evolutions of the vertical profile of aerosol extinction coefficient and PDR are shown in Figure 6. PDR is an effective parameter to separate the contribution of the more spherical particles from the ones due to dust-like aerosols (e.g. Chazette et al., 2012b). Between 16 and 19 June the PDR value is between 10 and 27%, which is representative of non-spherical dust-like aerosols (Müller et al., 2007; Tesche et al., 2011) as identified in Figure 4a for *BER* between ~0.021 and $0.028\ sr^{-1}$. Except between 26 and 28 June, the aerosol content is dominated by spherical particles. Between 26 and 28 June a depolarizing layer is observed between ~5 and 7 km amsl. The PDR ranges between 8 and 14% suggesting that dust aerosols were mixed with other aerosol sources or were processed during their transport to Menorca. We will further discuss this case in section 4. When considering the temporal evolution of AOT also given in Figure 6a, we note that lidar- and sunphotometer-derived AOT significantly differ on several occasions, especially in the cloudy periods (11, 20, 24, 25 and 27 June). It is due to residual cloud layers in the lidar profiles, which are not seen on the line-of-sight of the sunphotometer, with a positive bias explained by the higher BER of these thin layers. In addition, from 26 to 28 June, the presence of high altitude aerosol layers also probably causes a strong heterogeneity of the aerosol BER in the tropospheric column (see Figure 2b), which may explain part of the previous discrepancies because the aerosol types may be very different against the altitude. This shows the limited relevance of the notion of column-equivalent BER in heterogeneous cases.

3.3. Evidence of contributions by aerosol type as discriminated by lidar

225 The temporal evolution of the observed aerosol species can be derived from the analysis of
226 the equivalent BER and PDR. Indeed, these two parameters, only calculated from the lidar
227 profiles, are sufficiently discriminating to identify the main aerosol types in most cases
228 (Burton et al., 2012). Three aerosol types are considered: i) dust-like aerosols with values of
229 BER and PDR centred on 0.022 sr^{-1} and 20%, respectively, ii) pollution aerosols with BER
230 and PDR centred on 0.015 sr^{-1} and 2%, respectively, and iii) marine aerosols with mean
231 values of BER and PDR centred on 0.04 sr^{-1} and 0%, respectively. For each aerosol type,
232 literature sometimes reports a large range of values, as shown in Tables 1 and 3 of Dieudonné
233 et al. (2015) for dust and pollution aerosols, respectively. These authors report at the same
234 wavelength BER from 0.013 to 0.026 sr^{-1} (resp. 0.011 to 0.017 sr^{-1}) and PDR from 13 to 25%
235 (resp. 3 to 5%) for pure dust or dusty mix (resp. pollution) aerosols. This range of values
236 includes the lidar observations performed by Groß et al. (2011) in Cape verde (off shore of
237 West Africa) with *BER* = 0.017-0.020 sr^{-1} (*PDR* = 24-27%). The same authors report BER
238 from 0.042 to 0.053 sr^{-1} and PDR from 1 to 2% for marine aerosols. Figure 7 gives the
239 temporal evolution of the aerosol type after defining a specific colour map as a function of
240 BER and PDR. The lidar profiles were here averaged during 1 hour with a vertical resolution
241 of ~30 m. The aerosol backscatter coefficient (ABC) is coded by colour density: the more
242 saturated, the larger the ABC (white corresponds to ABC = 0). A specific colour scale is
243 affected to the couple of variables BER and PDR during nighttime. As the inversion using the
244 N_2-Raman channel is not possible when the sun is up, the colour map has been only
245 associated with the PDR during daytime.

246 Such a graphic representation allows the refinement of the identification of the aerosol types
247 that are presented in Figure 4a. The higher BERs retrieved in Figure 4a between 19 and 26
248 June are due to a larger contribution of reflective aerosols in the lower layers, likely sea salt
249 particles, which may also be very hydrophilic. Pollution aerosols are present all along the

measurement period except during the dust event between 16 and 19 June. It is more difficult to attribute the layer above 5 km amsl during the night of 26-27 June to a single aerosol source because depolarization is observed simultaneously with low BER. This layer arrives above a layer of biomass burning or polluted aerosols which spread between ~3 and 5 km amsl. A succession of pollution plumes originated from different locations along the Spanish coast contributes to the aerosol pollution load in the lower free troposphere over Menorca according to the air mass trajectories (not shown). The intermittent plumes, lifted as the PBL develops over Spain each afternoon, explain the periodic behavior observed in Figure 4a for the temporal evolution of the column-equivalent BER. However for the 26-27 June period the long range transport, revealed by the backtrajectories discussed hereafter, also shows a link with the North American biomass burning aerosol sources. Note that long range transport of biomass burning aerosols has always demonstrated to be a significant aerosol source over Europe (e.g. Fiebig et al., 2003; Müller et al., 2005). This temporal evolution of aerosol types based on the unique analysis of the lidar data is quite consistent with the column-integrated observations of the AERONET sunphotometer, as discussed in section 3.1 and reported in Figure 3.

3.4. Regional representativeness as seen by spaceborne measurements

The observations conducted from the Menorca Island station are relevant to the local atmospheric column. In the following we put them in a more regional context using the measurements performed by SEVIRI (e.g. Bennouna et al., 2009) and the spaceborne instruments Moderate Resolution Imaging Spectroradiometers (MODIS; Salmonson et al., 1989; King et al., 1992; http://modis.gsfc.nasa.gov). The MODIS data above land (few data are available above sea due to sun-glitter) and the SEVIRI data above sea are combined in a single map to check the reliability in terms of continuity between sea and continent.

The spatial resolution of the MYD04_L2 product of MODIS is 10 x 10 km^2 at nadir. The predicted uncertainty on the AOT at 550 nm over land is $\pm 0.15 \cdot AOT \pm 0.05$. The spatial and temporal resolutions of SEVIRI measurements are 10 x 10 km^2 and 15 minutes, respectively. The uncertainty on the SEVIRI-derived AOT is very dependent on the aerosol type (Bennouna et al., 2009). Compared to AERONET products from coastal stations, Thieuleux et al. (2005) do not highlight any significant bias on the AOT at 550 nm derived from SEVIRI for values between ~0.07 and 1. Their comparison based on observations in 2003 indicates that the SEVIRI AOT product is of somewhat lower quality at the sunphotometer sites directly affected by a desert dust plume from northern Africa. This is attributed to the fact that the aerosol models used to compute the look-up table does not include a specific desert dust model. Bréon et al. (2011) report a bias of 0.07 from their more exhaustive evaluation with AERONET sunphotometers over the period from June 2005 to December 2010. From a similar linear fitting between MODIS and AERONET, they found a smaller bias of ~0.02 and a correlation slope close to 1.

Figure 8 shows the inter-comparison between quarter-hourly products from SEVIRI and from the coincident AERONET sunphotometer of Menorca, including the AOT at 550 nm (Figure 8a) and the Ångström exponent (Figure 8b, computed between 630 and 810 nm, and 675 and 870 nm for SEVIRI and the sunphotometer, respectively). For the AOT, a linear least square fit highlights a significant deviation from the 1:1 relationship with a factor of 0.65. The additive bias is low, positive and close to 0.03. The mean rmse is ~0.066. The main discrepancies are mostly observed for the highest AOTs, occurring between 17-19 and 26-28 June when marine and dust aerosol are mixed and when biomass burning aerosols arrived above the site. The latter case is likely also associated with aerosol mixing. The discrepancies can be due to the resulting difficulty of the inversion process to identify a proper aerosol model, even for dust particles which never completely prevail in terms of AOT. We note the

299 larger dispersions for the mixing of marine particles with dust or pollution aerosols. In the
300 following, we have corrected by -35% the SEVIRI AOT_{550} product. Whereas the
301 sunphotometer-derived Ångström exponent seems coherent with our previous classification,
302 our results suggest that the SEVIRI Ångström exponent product (Figure 8b) relatively large
303 discrepancies at all AOT (although less at larger values), mostly related to aerosol type, and
304 this microphysical properties. The dispersion is lower for the dust (red in the figure) and
305 biomass burning (brown in the figure) events, but with overestimation and underestimation,
306 respectively. Consequently, the SEVIRI-derived AOT_{550} product over ocean, that relies on the
307 evaluated Angström exponent, should be carefully checked before use. Note that these
308 conclusions on both AOT and Ångström exponent cannot be generalized to other areas or
309 other time periods without further investigation.

310 The situations with the strongest AOT contrasts above the western Mediterranean basin are
311 shown in Figure 9. We can notice the very good continuity, after the correction of the
312 SEVERI-derived AOT, between sea and continent (MODIS-derived AOT). The main aerosol
313 events are linked with either the highest PDR observed between 16 and 19 June, or the highest
314 altitude transport (above 5 km amsl) between 26 and 28 June. The first event is due to desert
315 dust aerosols off the Moroccan and Algerian coasts (see also Figure 4). The second event
316 reveals a plume crossing the Mediterranean from North to South and will be discussed
317 hereafter. It is associated with a decrease of the BER after 26 June as shown in Figure 4a after
318 26 June.

319 **4. Discussion**

320 The pollution transport events observed at Menorca in the first part of the campaign, 12-18
321 June (Figure 4), are associated with the lowest values of the BER. To investigate their origins,
322 we ran the HYbrid Single-Particle Lagrangian Integrated Trajectory (HYSPLIT) model
323 (Draxler and Rolph, 2014) with 3-hourly archived meteorological data provided by the US

National Center for Environmental Prediction (NCEP) Global Data Assimilation System (GDAS) at the horizontal resolution of 0.5°. Two-day back-trajectories (not shown) clearly trace those polluted air masses back to Spain. Still in the same period, we note an increase of the BER during nighttime. It may be due to a higher relative contribution of hygroscopic aerosols below 1 km amsl as explained in section 3. Between 18 and 26 June (Figure 4), the BER reaches ~0.04 sr^{-1} (LR = 25 sr) as observed by Flamant et al. (2000) for marine aerosols over the open ocean. Nevertheless, we also note weak-medium surface wind speeds between 2 and 8 m s^{-1} not favourable to a strong contribution of sea salt particles in the lower troposphere.

Satellite data show the arrival of an African dust plume from the Alboran Sea over the Balearic Islands starting slowly on 15 June and leaving Menorca on 19 June. The AOT slightly increases from 16 to 18 June, when the densest part of the dust plume passes over the Menorca Island, to reach AOT_{355} = 0.25±0.05. As highlighted by 3-day back-trajectories (not shown), the dust plume came from Morocco and Algeria, as also illustrated by the satellite image in Figure 9a. Moreover, measurements of the Cloud-Aerosol LIdar with Orthogonal Polarization (CALIOP, PC-SCI-202.03, Vaughan et al., 2004) on 16 June highlight dust aerosols below 37.3° of latitude and polluted-dust aerosols above this latitude, which confirm the classification given in Figure 7. In the dust layer above 1 km amsl, the PDR is 20±5% and the mean BER (LR) is 0.024±0.002 sr^{-1} (~ 41.7±4 sr). Note that, as shown Figure 2a and previously discussed, the BER significantly evolves within the low and meddium troposphere from 0.04 sr^{-1} (LR = 25 sr) in the MBL to ~0.020-0.025 sr^{-1} (LR ~ 50-40 sr) in the dust layer situated above ~2 km amsl. A relative peak is observed in the BER profile between 1 and 2 km amsl associated with smaller values of the aerosol extinction coefficient (Figure 6). This intermediate layer is associated with PDR < 2% and may be mainly affected by both marine and pollution aerosols.

The high-altitude aerosol event observed between 4 and 7 km amsl above the western Mediterranean basin from 26 to 28 June is not usual in its nature since it results from a very turbid plume (AOT_{550} >0.6) arriving from the NE Atlantic as visible on the Bay of Biscay on 26 June in Figure 10. Formenti et al. (2002) have already documented with airborne measurements such an occurrence of 10-day aged haze layers from Canadian fires over the eastern Mediterranean in August 1998. Seven days-back trajectories have been computed with the HYSPLIT model (Figure 10). The back trajectories are superimposed on a MODIS AOT image combining data from 24 June, 2013. Dense aerosol plumes appear all along a transport pathway over the Northern Atlantic, with a dark red colour associated with AOT_{550} values larger than 1. Note that the AOT even reaches 5 for many pixels, maybe because cloud contribution is also included as can be seen in the true colour image available on https://earthdata.nasa.gov/labs/worldview/. As shown in Figure 10, the biomass burning plume observed at 6 km over Menorca on 27 June crossed the Atlantic Ocean at altitudes between 4 and 8 km amsl. The plume is associated with forest burning occurring in Canada and Colorado.

The possible source regions are discussed in detail in the companion paper of Ancellet et al. (2016). It includes contributions from two different plumes: biomass burning aerosol from North America and dust transported westward over the Atlantic by the trade winds. Trajectories from the other plume detected close to 4 km amsl over Menorca by the lidar on 28 June (Figure 6) also come from North America with little contribution from the Atlantic Saharan dust. The North American aerosol event of 26-27 June is characterized by AOT_{355} = 0.18±0.16 above Menorca. It represents ~50% of the total columnar AOT (AOT_{355} = 0.41±0.12) encountered during this day. It is associated with a moister air mass, with a WVMR close to 1-2 g/kg, comparatively to the clean free mid-troposphere (0.5 g/kg), as derived from the H_2O-Raman lidar channel. The uplifting of air masses from the lower

374 troposphere occurs either above the continental US or above the Atlantic ocean as discussed
375 in Ancellet et al. (2016). The equivalent *BER* has been assessed to be 0.023±0.002 sr^{-1}
376 (LR ~ 43.5±4 sr) and corresponds about to the mean value of the vertical profile of BER
377 given in Figure 2b. As previously, the value retrieved in the MBL correspond to marine
378 aerosols. The BER in the mixture of biomass burning aerosol and dust is determined as
379 0.025±0.002 sr^{-1} (*LR* ~ 40±3 sr) with a PDR between 8 and 14%. PDR values between 8%
380 and 18% were measured over Cyprus by the lidar of Limassol (Nisantzi et al., 2014) for
381 almost fresh biomass burning aerosols mixed with dust-like particles uplifted by thermal
382 convection and transported above the lidar site. However, the dust observed over Cyprus
383 presents a larger BER than the one generally derived over Sahara. Groß et al. (2011) also
384 report larger values of PDR (18-22%) for a mixture of biomass burning and Saharan dust
385 aerosol over Cape Verde with BER between 0.014 and 0.016 sr^{-1} (LR between 60 and 70 sr).
386 In our case, the aerosols are more aged (at least 7 days) and may be more spherical due to
387 water vapour condensation during transport over the Atlantic Ocean. We note cloud formation
388 along some filaments created from the initial plume (not shown). Such a phenomenon
389 decreases the PDR. Nevertheless, the value of PDR is higher and may indicate the presence of
390 dust-like particles within the biomass burning plume. The high vertical resolution of the
391 CALIOP lidar (30-60 m) can be processed to derive aerosol type and optical properties of the
392 aerosol layers (e.g. Vaughan et al., 2004; Thomason et al., 2007; Kim et al., 2008; Berthier et
393 al., 2006) as the PDR. The 8-14% PDR measured at 355 nm by the WALI lidar appears
394 comparable to the 10% PDR at 532 nm observed by CALIOP (the ground track is given in
395 Figure 9d) off the Mediterranean Spanish coast at 1°E in a layer between 38°N and 39°N on
396 28 June, 0200 UTC (see Ancellet et al. 2016 in the same issue). Over the Atlantic Ocean (24
397 June), the aerosol plume is identified by CALIOP measurements either of smoke type or of
398 polluted dust type.

5. Conclusion

Aerosol optical properties in the tropospheric column were derived from the measurements performed continuously, during three weeks in June and early July 2013, at Menorca Island during the Chemistry-Aerosol Mediterranean Experiment / Aerosol Direct Radiative Effect in the Mediterranean (ChArMEx/ADRIMED) special observation period (SOP-1a). The measurements sampled air masses with very different aerosol content and a large range of optical thicknesses (AOT_{355} = 0.29±0.17), which has been shown as representative of the years 2011 to 2013 (AOT_{355} = 0.24±0.15). There are only a few cases where the aerosol layers are not composed of a mixture of different aerosol types. They are originating from the surrounding sea, the Spanish coastal cities, the North Africa deserts and even distant forest fires in North America. We have noted that the complex mixing of aerosols likely impact the retrieval of the AOT from SEVIRI leading to a relative bias close to 35%.

The instrumental synergy, coupling either the sunphotometer or the N_2-Raman channel with the elastic channel, allows a well-constrained processing of the lidar measurements, from which we were able to follow the evolution of the aerosol optical properties between night and day. In particular, the continuity of column-equivalent BER measurements is ensured. Lidar observations allowed locating scattering layers in the troposphere, and in particular identifying a complex aerosol transport from North America in the middle troposphere (between 2 and 7 km amsl). Air masses took between 5 and 7 days to arrive over the Mediterranean Sea. There has been a great variability in the nature of aerosols in the troposphere during this period from 26 to 28 June, 2013. This variability is evidenced by the BER profile estimated from the Raman lidar WALI, with a strong variance (BER (LR) = 0.024±0.008 sr^{-1} (~ 41.7±14 sr), above 4 km amsl and < 0.02 sr^{-1} (> 50 sr) between 2 and 4 km amsl). However, such variability has weak impact on the AOT measurements, be it during nighttime or daytime. We have also observed the presence of depolarizing particles

(*PDR* ~8-14% @355 nm) in a biomass burning plume originating from North America corresponding to Saharan dust re-circulated over the Atlantic Ocean, as discussed in the companion paper by Ancellet et al. (2016).

These results show that an assessment of the radiative budget of aerosols over the western Mediterranean basin can be easily performed by considering the average optical properties of the particles. Nevertheless, for the evaluation of atmospheric heating rates and possible associated effects on cloud formation, account must be taken of the single scattering albedo, which is linked to the vertical evolution of the aerosol types given by our classification. Moreover, the single scattering albedo may be constrained by the lidar-derived BER as in Randriamiarisoa et al. (2004) or Raut and Chazette (2008). The latter has indeed been shown in this campaign to be very variable, both in time and altitude, due to the mixing of very different aerosol contributions over the Mediterranean Sea.

Acknowledgements. This work was supported by the French space agency (CNES) and the Commissariat à l'Energie Atomique (CEA). The campaign at Menorca was also supported by CNRS/INSU and Météo-France through the MISTRALS/ChArMEx programme, and by the Spanish Ministry of Science and Innovation and FEDER funds under the projects TEC2012-34575, UNPC10-4E-442 and CGL2011-13580-E/CLI. Matthieu Jeannot from LPC2E, François Dulac and Sahar Hassanzadeh from LSCE are acknowledged for their technical help during the campaign. Juan Ramon Moreta Gonzalez and Miguel Angel Heredia Jodar from AEMET are acknowledged for AERONET data from Palma.

6. References

Ancellet, A., Pelon, J., Totems, J., Chazette, P., Bazureau, A., Sicard, M., Di Iorio, T., Dulac, M., and Mallet, M.: Long range transport and mixing of aerosol sources during the 2013 North American biomass burning episode : analysis of multiple lidar observations in the Western Mediterranean basin, accepted to Atmos. Chem. Phys., this special issue, 2016.

449 Ångström, A.: The parameters of atmospheric turbidity, Tellus, 16, 64-75, 1964.

450 Bennouna, Y. S., de Leeuw, G., Piazzola, J., and Kurmierczyk-Michulec, J.: Aerosol remote
451 sensing over the ocean using MSG-SEVIRI visible images, J. Geophys. Res., 114, *D23203*,
452 doi: 10.1029/2008JD011615, 2009.

453 Berthier, S., Chazette, P., Couvert, P., Pelon, J., Dulac, F., Thieuleux, F., Moulin, C., and
454 Pain, T. : Desert dust aerosol columnar properties over ocean and continental Africa from
455 Lidar in-Space Technology Experiment (LITE) and Meteosat synergy, J. Geophys. Res., 111,
456 D21202, doi:10.1029/2005JD006999, 2006.

457 Blanchard, C.D., Woodcock, A.H., and Cipriano, R.J., The Vertical Distribution of
458 Concentration of Sea Sealt in the Marine Atmosphere near Hawaii, Tellus, 36B, 118-125,
459 1984.

460 Bréon, F.-M. M., Vermeulen, A., and Descloitres, J.: An evaluation of satellite aerosol
461 products against sunphotometer measurements, Remote Sens. Environ., 115(12), 3102–3111,
462 doi:10.1016/j.rse.2011.06.017, 2011.

463 Burton, S. P., Ferrare, R. A., Hostetler, C. A., Hair, J. W., Rogers, R. R., Obland, C. F.,
464 Butler, M. D., Cook, A. L., Harper, D. B., and Froyd, K. D.: Aerosol classification using
465 airborne High Spectral Resolution Lidar measurements—methodology and examples Atmos.
466 Meas. Technol., 5, 73–98, 2012.

467 Cachier, H., Aulagnier, F., Sarda, R., Gautier, F., Masclet, P., Besombes, J.-L., Marchand, N.,
468 Despiau, S., Croci, D., Mallet, M., Laj, P., Marinoni, A., Deveau, P.-A., Roger, J.-C., Putaud,
469 J.-P., Van Dingenen, R., Dell'Acqua, A., Viidanoja, J., Martins-Dos Santos, S., Liousse, C.,
470 Cousin, F., Rosset, R., Gardrat, E., and Galy-Lacaux, C.: Aerosol studies during the
471 ESCOMPTE experiment: An overview, Atmos. Res., 74, 547–563, 2005.

472 Chazette, P.: The monsoon aerosol extinction properties at Goa during INDOEX as measured
473 with lidar, J. Geophys. Res., 108(D6), 4187, doi:10.1029/2002JD002074, 2003.

474 Chazette, P., Couvert, P., Randriamiarisoa, H., Sanak, J., Bonsang, B., Moral, P., Berthier, S.,
475 Salanave, S., and Toussaint, F.: Three-dimensional surveyof pollution during winter in French
476 Alps valleys, Atmos. Environ., 39, 1035-1047, 2005a.

477 Chazette, P., Randriamiarisoa, H., Sanak, J., Couvert, P., and Flamant, C.: Optical properties
478 of urban aerosol from airborne and ground-based in situ measurements performed during the
479 Etude et Simulation de la Qualité de l'air en Ile de France (ESQUIF) program, J. Geophys.
480 Res., 110(D2), D02206, doi:10.1029/2004JD004810, 2005b.

481 Chazette, P., Dabas, a., Sanak, J., Lardier, M. and Royer, P.: French airborne lidar
482 measurements for Eyjafjallajökull ash plume survey, Atmos. Chem. Phys., 12(15), 7059–
483 7072, doi:10.5194/acp-12-7059-2012, 2012a.

484 Chazette, P., Bocquet, M., Royer, P., Winiarek, V., Raut, J. C., Labazuy, P., Gouhier, M.,
485 Lardier, M., and Cariou, J. P.: Eyjafjallajökull ash concentrations derived from both lidar and
486 modeling, J. Geophys. Res. Atmos., 117, D00U14, doi:10.1029/2011JD015755, 2012b.

Chazette, P., Marnas, F., and Totems, J.: The mobile Water vapor Aerosol Raman LIdar and its implication in the framework of the HyMeX and ChArMEx programs: application to a dust transport process, Atmos. Meas. Tech., 7(6), 1629–1647, doi:10.5194/amt-7-1629-2014, 2014.

Cros, B., Durand, P., Cachier, H., Drobinski, Ph., Fréjafon, E., Kottmeier, C., Perros, P., Peuch, V., Ponche, J.-L., Robin, D., Said, F., Toupance, G., and Wotham, H.: The ESCOMPTE Program: an overview, Atmos. Res., 69, 241–279, 2004.

Dieudonné, E., Chazette, P., Marnas, F., Totems, J., and Shang, X.: Lidar profiling of aerosol optical properties from Paris to Lake Baikal (Siberia), Atmos. Chem. Phys., 15(9), 5007–5026, doi:doi:10.5194/acp-15-5007-2015, 2015.

Draxler, R. R. R. and Rolph, G. D. D.: HYSPLIT (HYbrid Single-Particle Lagrangian Integrated Trajectory) Model access via NOAA ARL READY Website, available at: http://www.arl.noaa.gov/HYSPLIT.php (last access: november 2015). NOAA Air Resources Laboratory, College Park, MD, 2014.

Di Iorio, T., di Sarra, A., Junkermann, W., Cacciani, M., Fiocco, G., and Fuà, D.: Tropospheric aerosols in the Mediterranean: 1. Microphysical and optical properties, J. Geophys. Res., 108, D02201, doi: 10.1029/2002JD002815, 2003.

Dubovik, O. and King, M. D.: A flexible inversion algorithm for retrieval of aerosol optical properties from Sun and sky radiance measurements, J. Geophys. Res. Atmos., 105(D16), 20673–20696, doi:10.1029/2000JD900282, 2000.

Dulac, F., and Chazette, P.: Airborne study of a multi-layer aerosol structure in the eastern Mediterranean observed with the airborne polarized lidar ALEX during a STAAARTE campaign (7 June 1997), Atmos. Chem. Phys., 3, 1817–1831, doi:10.5194/acp-3-1817-2003, 2003.

Flamant, C., Pelon, J., Chazette, P., Trouillet, V., Quinn, P. K., Frouin, R., Bruneau, D., Francois Leon, J., Bates, T. S., Johnson, J., and Livingston, J.: Airborne lidar measurements of aerosol spatial distribution and optical properties over the Atlantic Ocean during a European pollution outbreak of ACE-2, Tellus B, 52(2), 662–677, doi:10.1034/j.1600-0889.2000.00083.x, 2000.

Fiebig, M., Stohl, A., Wendisch, M., Eckhardt, S. and Petzold, A.: Dependence of solar radiative forcing of forest fire aerosol on ageing and state of mixture, Atmos. Chem. Phys., 3(3), 881–891, doi:10.5194/acp-3-881-2003, 2003.

Formenti, P., Boucher, O., Reiner, T., Sprung, D., Andreae, M. A., Wendisch, M., Wex, H., Kindred, D., Tzortziou, M., Vasaras, A., and Zerefos, C.: STAAARTE-MED 1998 summer airborne measurements over the Aegean Sea. 2. Aerosol scattering and absorption, and radiative calculations, J. Geophys. Res., 107, 4451, doi:10.1029/2001JD001536, 2002.

Giorgi, F. and Lionello, P.: Climate change projections for the Mediterranean region, Glob. Planet. Change, 63(2-3), 90–104, doi:10.1016/j.gloplacha.2007.09.005, 2008.

525 Gobbi, G.P., Barnaba, F., Blumthaler, M., Labow, G., and Herman, J.L.: Observed effects of
526 particles nonsphericity on the retrieval of marine and desert dust aerosol optical depth by
527 lidar, Atmos. Res., 61, 1-14, 2000.

528 Groß, S., Tesche, M., Freudenthaler, Toledano, C., V., Wiegner, Ansmann, A., Althausen, D.,
529 and Seefeldner, M.: Characterization of Saharan dust, marine aerosols and mixtures of
530 biomass-burning aerosols and dust by means of multi-wavelength depolarization and Raman
531 lidar measurements during SAMUM 2, Tellus, 63B, 706-724, 2011.

532 Hamonou, E., Chazette, P., Balis, D., Dulac, F., Schneider, X., Galani, E., Ancellet, G. and
533 Papayannis, A.: Characterization of the vertical structure of Saharan dust export to the
534 Mediterranean basin, J. Geophys. Res., 104(D18), 22257, doi:10.1029/1999JD900257, 1999.

535 Holben, B. N., Eck, T. F., Slutsker, I., Tanré, D., Buis, J. P., Setzer, A., Vermote, E. F.,
536 Reagan, J. A., Kaufman, Y. J., Nakajima, T., Lavenu, F., Jankowiak, I., and Smirnov, A.:
537 AERONET – A federated instrument network and data archive for aerosol characterization,
538 Remote Sens. Environ., 66, 1–16, 1998.

539 IPCC, 2014: Climate Change 2014: Impacts, Adaptation, and Vulnerability. Part A: Global
540 and Sectoral Aspects. Contribution of Working Group II to the Fifth Assessment Report of the
541 Intergovernmental Panel on Climate Change, Field, C.B., Barros, V.R., Dokken, D.J., Mach,
542 K.J., Mastrandresa, M.D., Bilir, T.E., Chatterjee, M., Ebi, K.L., Estrada, Y.O., Genova, R.C.,
543 Girma, B., Kissel, E.S., Levy, A.N., MacCracken, S., Mastrandrea, P.R., and White, L.L.
544 (eds), Cambridge University Press, Cambridge, United Kingdom and new York, NY, USA,
545 1132 pp.

546 Kim, S. W., Berthier, S., Raut, J.-C., Chazette, P., Dulac, F., and Yoon, S.-C.: Validation of
547 aerosol and cloud layer structures from the space-borne lidar CALIOP using a ground-based
548 lidar in Seoul, Korea, Atmos. Chem. Phys., 8, 3705–3720, doi:10.5194/acp-8-3705-2008,
549 2008.

550 King, M. D., Kaufman, Y. J., Menzel, P. and Tanré, D.: Remote-sensing of cloud, aerosol,
551 and water-vapor properties from the Moderate Resolution Imaging Spectroradiometer
552 (MODIS), IEEE Trans. Geosci. Remote Sensing, 30, 2-27, 1992.

553 Klett, J. D.: Lidar inversion with variable backscatter/extinction ratios, Appl. Opt., 24(11),
554 1638, doi:10.1364/AO.24.001638, 1985.

555 Lelieveld, J., Berresheim, H., Borrmann, S., Crutzen, P.J., Dentener, F.J., Fischer, H.,
556 Feichter, J., Flatau, P.J., Heland, J., Holzinger, R., Korrmann, R., Lawrence, M.G., Levin, Z.,
557 Markowicz, K.M., Mihalopoulos, N., Minikin, A., Ramanathan, V., de Reus, M., Roelofs,
558 G.J., Scheeren, H.A., Sciare, J., Schlager, H., Schultz, M., Siegmund, P., Steil, B., Stephanou,
559 E.G., Stier, P., Traub, M.,Warneke, C., Williams, J., and Ziereis, H.: Global air pollution
560 crossroads over the Mediterranean, Science, 298, 794–799, 2002.

561 Levin, Z., Teller, A., and Ganor, E.: On the interactions of mineral dust, sea-salt particles, and
562 clouds: A measurement and modeling study from the Mediterranean Israeli Dust Experiment
563 campaign, J. Geophys. Res., 110, D05207, doi: 10.1029/2005JD005810, 2005.

564 Mallet, M., et al.: Overview of the Chemistry-Aerosol Mediterranean Experiment/Aerosol
565 Direct Radiative Forcing on the Mediterranean Climate (ChArMEx/ADRIMED) summer
566 2013 campaign, Atmos. Chem. Phys., this special issue, 2015.

567 Moulin C., Lambert, C. E., Dayan, U., Masson, V., Ramonet, M., Bousquet, P., Legrand, M.,
568 Balkanski, Y. J., Guelle, W., Marticorena, B., Bergametti, G., and Dulac, F.: Satellite
569 climatology of African dust transport in the Mediterranean atmosphere, J. Geophys. Res., 103,
570 13137–13144, 1998.

571 Müller, D., Mattis, I., Ansmann, A., Wandinger, U., Ritter, C. and Kaiser, D.: Raman lidar
572 observations of aged Siberian and Canadian forest fire smoke in the free troposphere over
573 Germany in 2003: Microphysical particle characterization, J. Geophys. Res., 110(D17),
574 D17201, doi:10.1029/2004JD005756, 2005.

575 Müller, D., Ansmann, A., Mattis, I., Tesche, M., Wandinger, U., Althausen, D., and Pisani,
576 G.: Aerosol-type-dependent lidar ratios observed with Raman lidar, J. Geophys. Res. Atmos.,
577 112, D16202, doi:10.1029/2006JD008292, 2007.

578 Nabat, P., Somot, S., Mallet, M., Chiapello, I., Morcrette, J. J., Solmon, F., Szopa, S., Dulac,
579 F., Collins, W., Ghan, S., Horowitz, L. W., Lamarque, J. F., Lee, Y. H., Naik, V., Nagashima,
580 T., Shindell, D. and Skeie, R.: A 4-D climatology (1979-2009) of the monthly tropospheric
581 aerosol optical depth distribution over the Mediterranean region from a comparative
582 evaluation and blending of remote sensing and model products, Atmos. Meas. Tech., 6, 1287–
583 1314, doi:10.5194/amt-6-1287-2013, 2013.

584 Nabat, P., Somot, S., Mallet, M., Michou, M., Sevault, F., Driouech, F., Meloni, D., Di Sarra,
585 A., Di Biagio, C., Formenti, P., Sicard, M., Léon, J.-F., and M.-N. Bouin: Dust aerosol
586 radiative effects during summer 2012 simulated with a coupled regional aerosol–atmosphere–
587 ocean model over the Mediterranean, Atmos. Chem. Phys., 15, 3303-3326, doi: 10.5194/acp-
588 15-3303-201, 2015.

589 Nisantzi, A., Mamouri, R. E., Ansmann, A., and Hadjimitsis, D.: Injection of mineral dust
590 into the free troposphere during fire events observed with polarization lidar at Limassol,
591 Cyprus, Atmos. Chem. Phys., 14(22), 12155–12165, doi:10.5194/acp-14-12155-2014, 2014.

592 Papayannis, A., Amiridis, V., Mona, L., Tsaknakis, G., Balis, D., Bösenberg, J., Chaikovski,
593 A., De Tomasi, F., Grigorov, I., Mattis, I., Mitev, V., Müller, D., Nickovic, S., Pérez, C.,
594 Pietruczuk, A., Pisani, G., Ravetta, F., Rizi, V., Sicard, M., Trickl, T., Wiegner, M., Gerding,
595 M., Mamouri, R. E., D'Amico, G. and Pappalardo, G.: Systematic lidar observations of
596 Saharan dust over Europe in the frame of EARLINET (2000–2002), J. Geophys. Res.,
597 113(D10), D10204, doi:10.1029/2007JD009028, 2008.

598 Paronis, D., Dulac, F., Chazette, P., Hamonou, E., and Liberti, G. L.: Aerosol optical
599 thickness monitoring in the Mediterranean, J. Aerosol Sci., 29, S671–S672, 1998.

600 Randriamiarisoa, H., Chazette, P., and Megie, G.: Retrieving the aerosol single-scattering
601 albedo from the NO 2 photolysis rate coefficient, Tellus B, 56(2), 118-127,
602 doi:10.3402/tellusb.v56i2.16408, 2004.

603 Raut, J.-C., and Chazette, P.: Radiative budget in the presence of multi-layered aerosol
604 structures in the framework of AMMA SOP-0, Atmos. Chem. Phys., 8(4), 12461–12528,
605 doi:10.5194/acpd-8-12461-2008, 2008.

606 Royer, P., Chazette, P., Lardier, M., and Sauvage, L.: Aerosol content survey by mini N2-
607 Raman lidar: Application to local and long-range transport aerosols, Atmos. Environ., 45(39),
608 7487–7495, 2011.

609 Tesche, M., Gross, S., Ansmann, A., Müller, D., Althausen, D. and Freudenthaler, V., and
610 Esselborn, M.: Profiling of Saharan dust and biomass-burning smoke with multiwavelength
611 polarization Raman lidar at Cape Verde, Tellus B, 63, 649–676,
612 doi:10.1111/j.16000889.2011.00548.x, 2011.

613 Thieuleux, F., Moulin, C., Bréon, F. M., Maignan, F., Poitou, J. and Tanré, D.: Annales
614 Geophysicae Remote sensing of aerosols over the oceans using MSG / SEVIRI imagery, ,
615 23(12), 1–8, 2005.

616 Thomason, L. W., Pitts, M. C., and Winker, D. M.: CALIPSO observations of stratospheric
617 aerosols: a preliminary assessment, Atmos. Chem. Phys., 7, 5283-5290, 2007.

618 Vaughan, M. A., Young, S. A., Winker, D. M., Powell, K. A., Omar, A. H., Liu, Z., Hu, Y.,
619 and Hostetler, C. A.: Fully automated analysis of space-based lidar data: An overview of the
620 CALIPSO retrieval algorithms and data products, Proc. SPIE Int. Soc. Opt. Eng., 5575, 16–
621 30, doi:10.1117/12.572024, 2004.

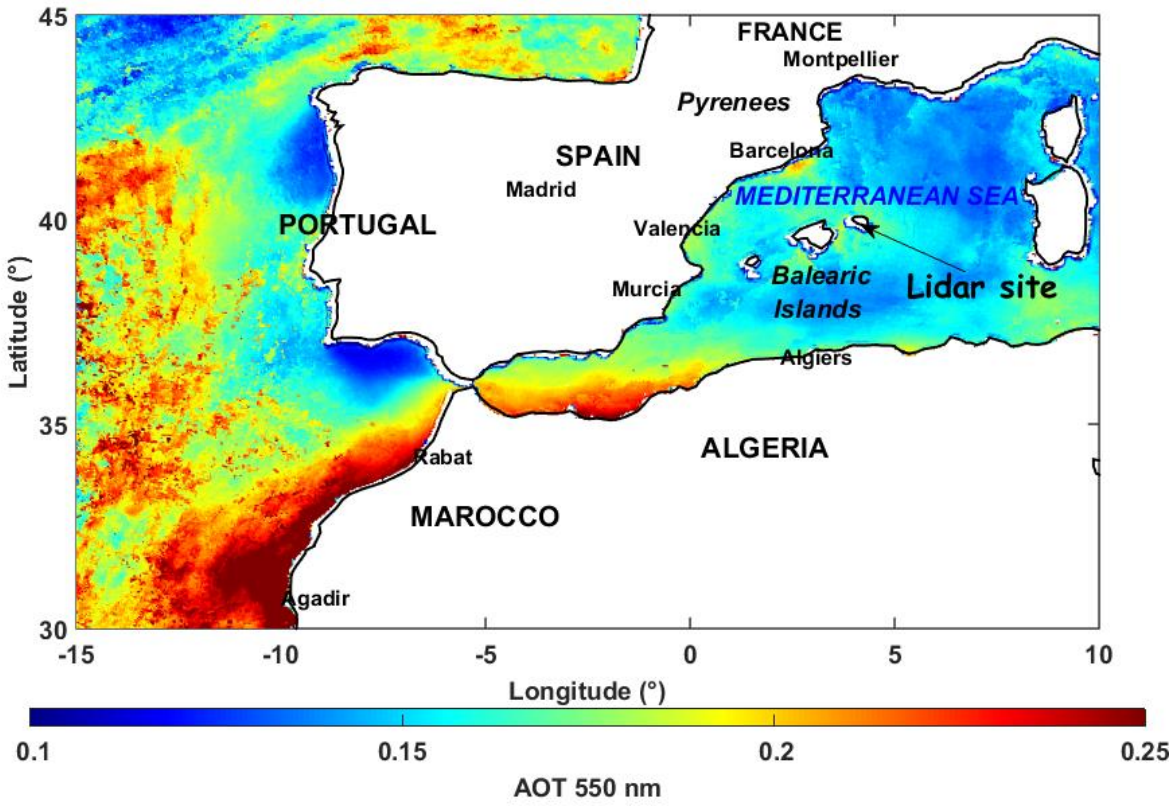

622

623 Figure 1: Location of the Cap d'en Font surface station on Menorca Island, on a map of the
624 MSG/SEVIRI-derived aerosol optical thickness at 550 nm over ocean, averaged over the
625 campaign period (10 June-3 July 2013, daytime).

a)

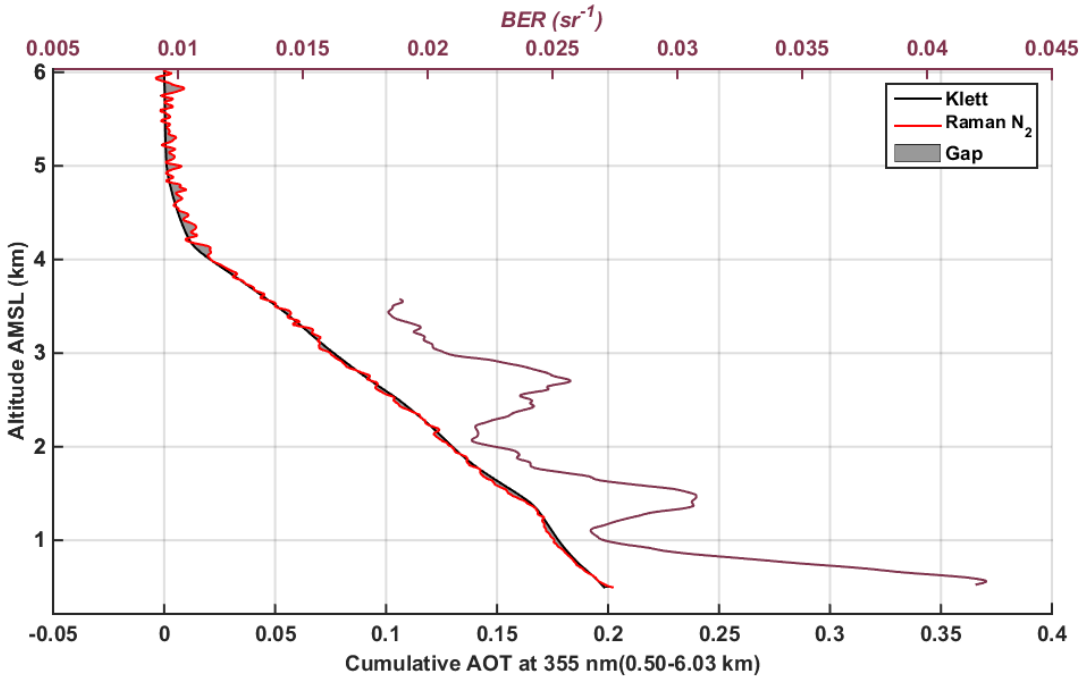

b)

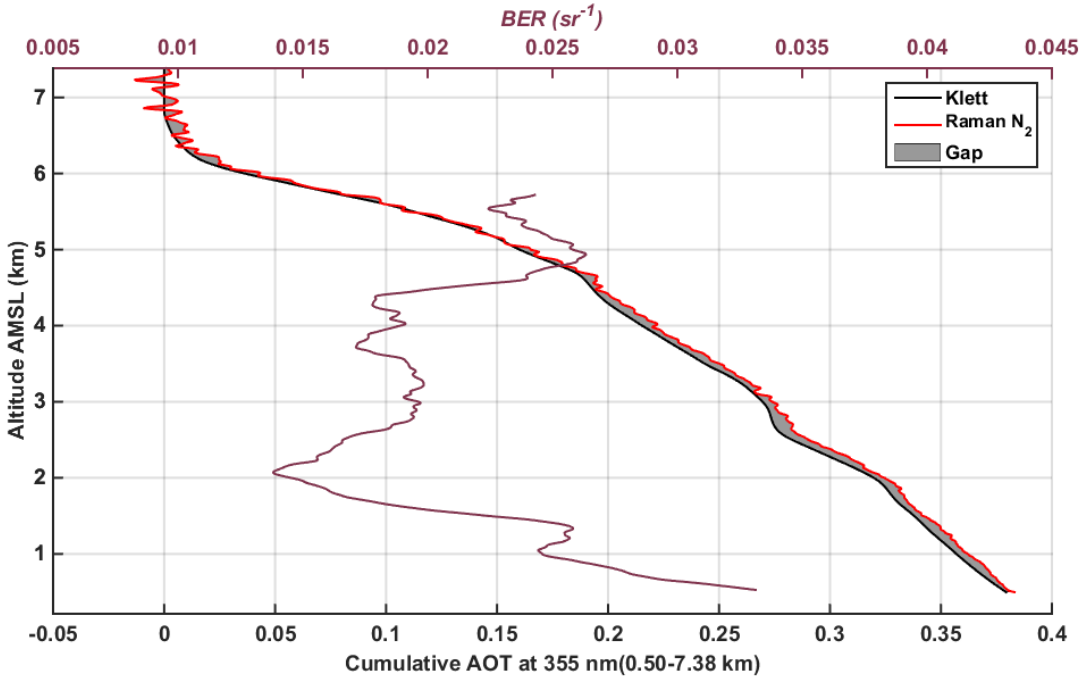

626 Figure 2: Result of the lidar inversion on the both the integrated AOT and the BER for the
627 elastic (Klett (1985) algorithm) and N_2-Raman channels: a) the nights of 16-17 June, and b)
628 the nights of 27-28 June. The grey area highlights the gap between the two approaches.

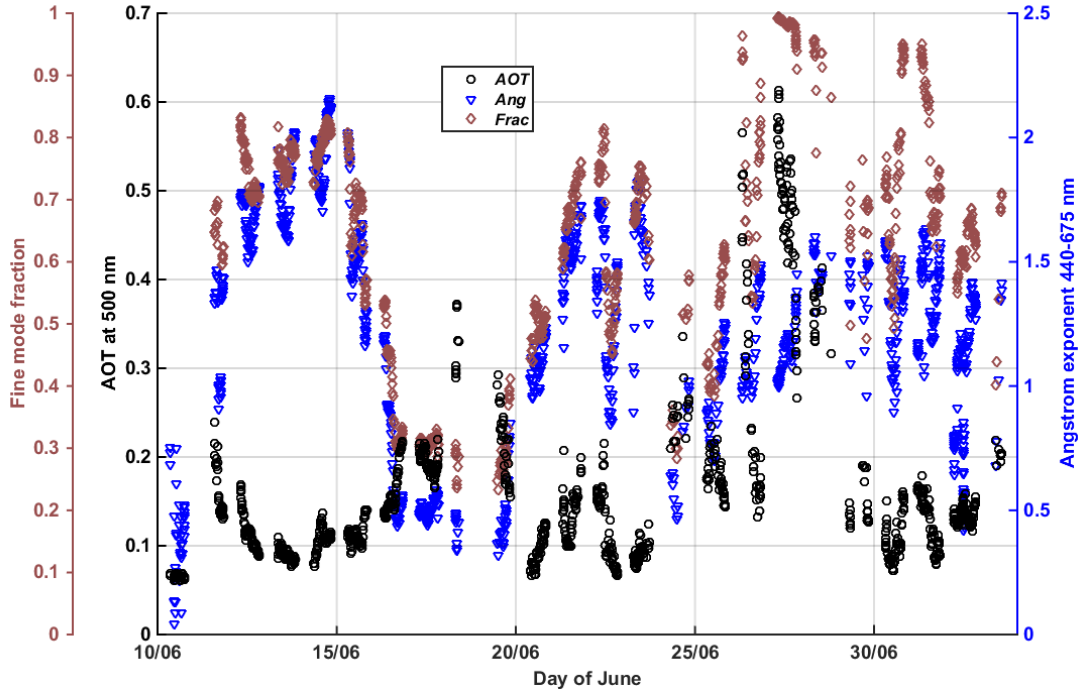

Figure 3: Temporal evolution between 10 June and 3 July 2013, local time, of the aerosol optical thickness at 500 nm (*AOT*), the Ångström exponent between 440 and 675 nm (*Ang*) and the fine mode fraction (*Frac*) as derived from the sunphotometer measurements at Cap d'en Font. The AERONET products are completed by the Microtops II manual sunphotometer measurements on 10 June.

a)

b)

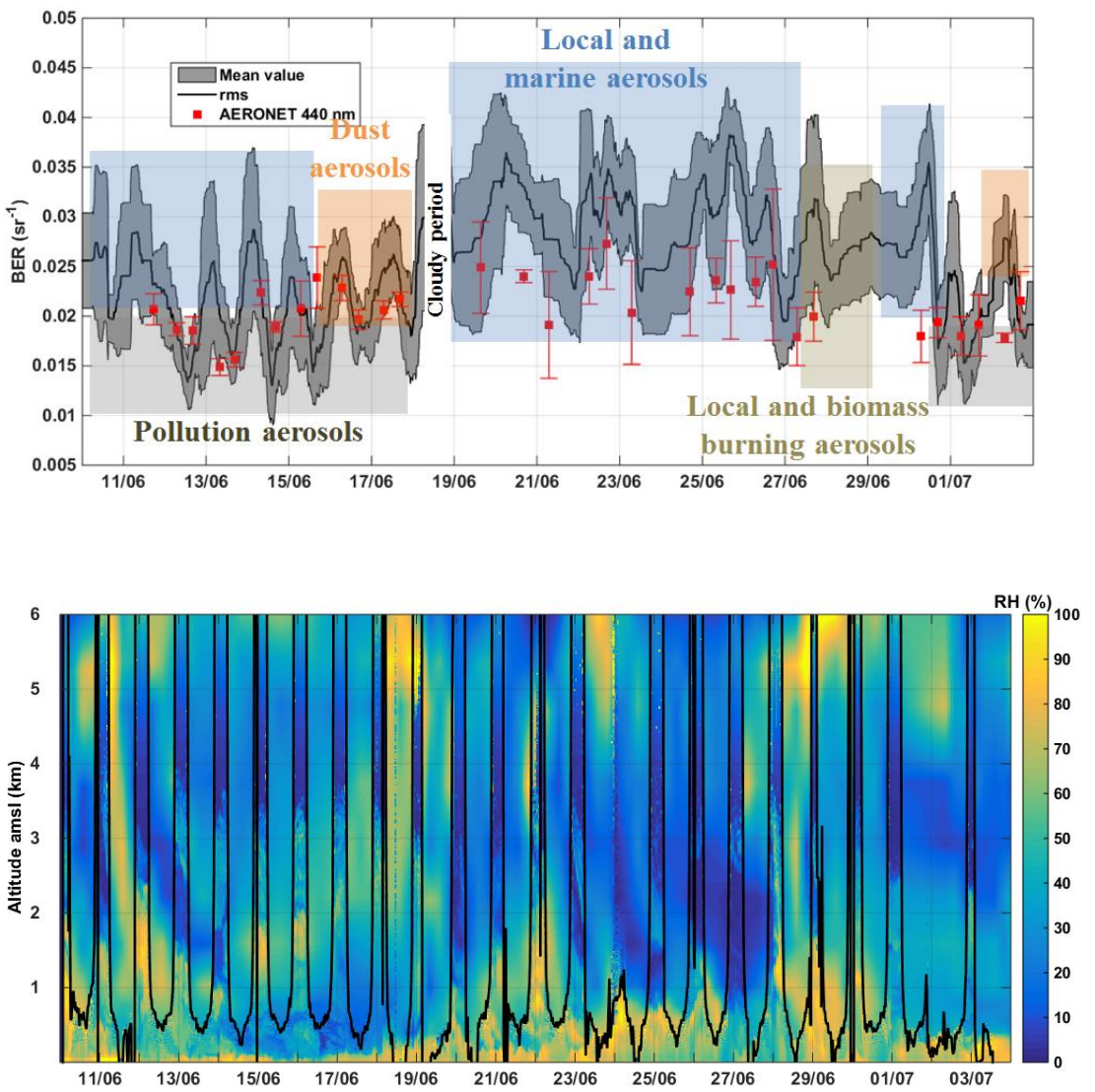

635 Figure 4: Temporal evolution of (a) the backscatter-to-extinction ratio (*BER*) and (b) the
636 relative humidity (RH) between 10 and 29 June 2013. In (a) the root mean square error (rmse)
637 is given by the grey area. The main aerosol categories have been identified in the figure as
638 pollution, dust, local, marine and biomass burning aerosols using *BER* and *PDR* values (see
639 text). The sunphotometer-derived BER is superimposed in red with its standard deviation
640 (variability over half a day). In (b) the RH is calculated from lidar measurements using the
641 thermodynamic temperature given by ECMWF analyses. During daytime the RH in the free
642 troposphere is that of ECMWF; the boundary between the two RH determinations is
643 highlighted by the continuous black line.

a)

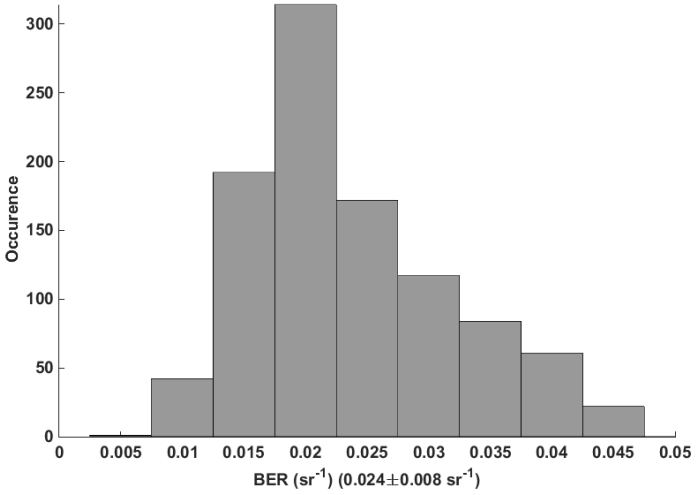
Occurence
0
50
100
150
200
250
300
0 0.005 0.01 0.015 0.02 0.025 0.03 0.035 0.04 0.045 0.05
BER (sr-1) (0.024±0.008 sr-1)

b)

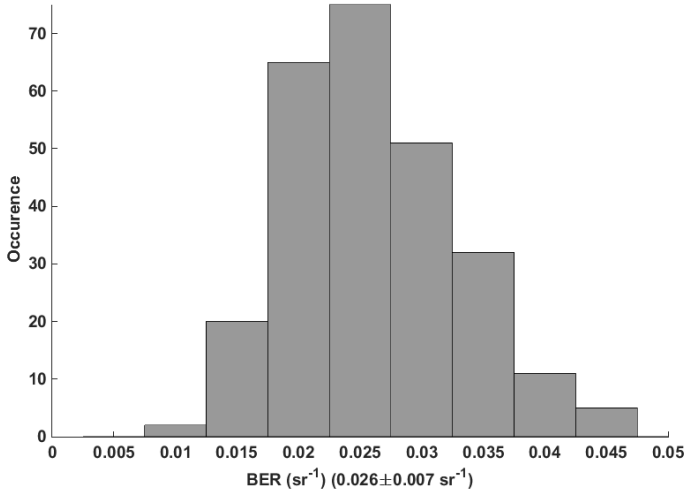
Occurence
0
10
20
30
40
50
60
70
0 0.005 0.01 0.015 0.02 0.025 0.03 0.035 0.04 0.045 0.05
BER (sr-1) (0.026±0.007 sr-1)

c)

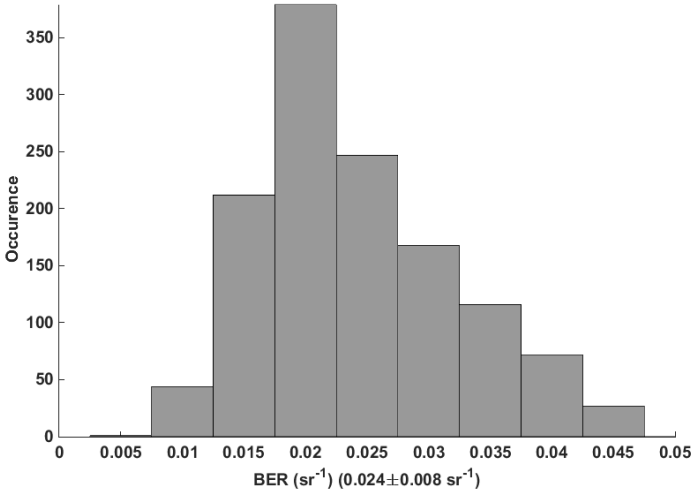
Occurence
0
50
100
150
200
250
300
350
0 0.005 0.01 0.015 0.02 0.025 0.03 0.035 0.04 0.045 0.05
BER (sr-1) (0.024±0.008 sr-1)

644 Figure 5: Backscatter-to-extinction ratio (*BER*) retrieved from a) the synergy of the WALI
645 lidar and the sunphotometer during daytime, b) the coupling between the elastic and N_2-
646 Raman channels during nighttime, and c) the synthesis of daytime and nighttime results.

a)

b)

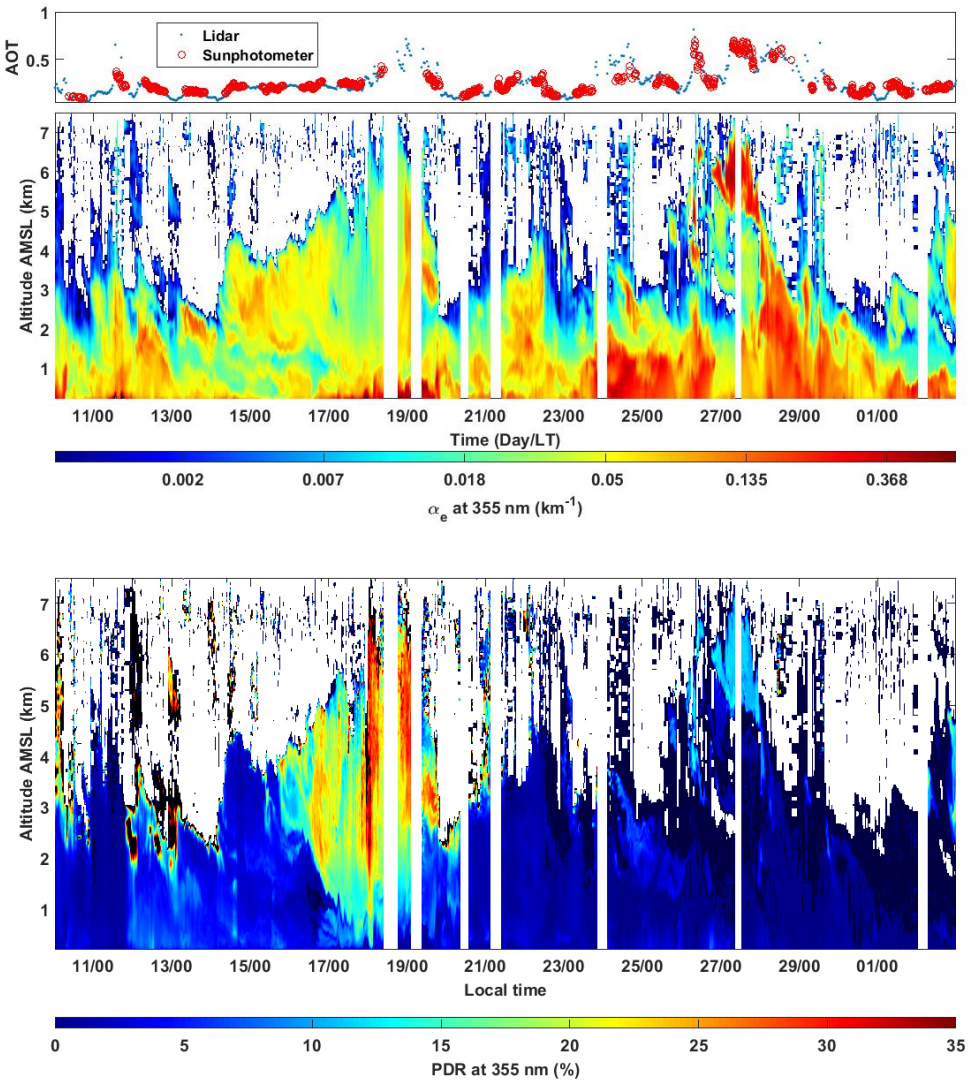

Figure 6: a) The temporal evolution of the vertical profile of the aerosol extinction coefficient at 355 nm (α_e). The top panel shows AOT at 355 nm derived from the sunphotometer (red circles) and lidar measurements (blue points). b) The temporal evolution of the particulate depolarization ratio vertical profile at 355 nm (*PDR*). Time white stripes correspond to periods filtered out by visual examination of the lidar signal to identify the occurrence of clouds.

a)

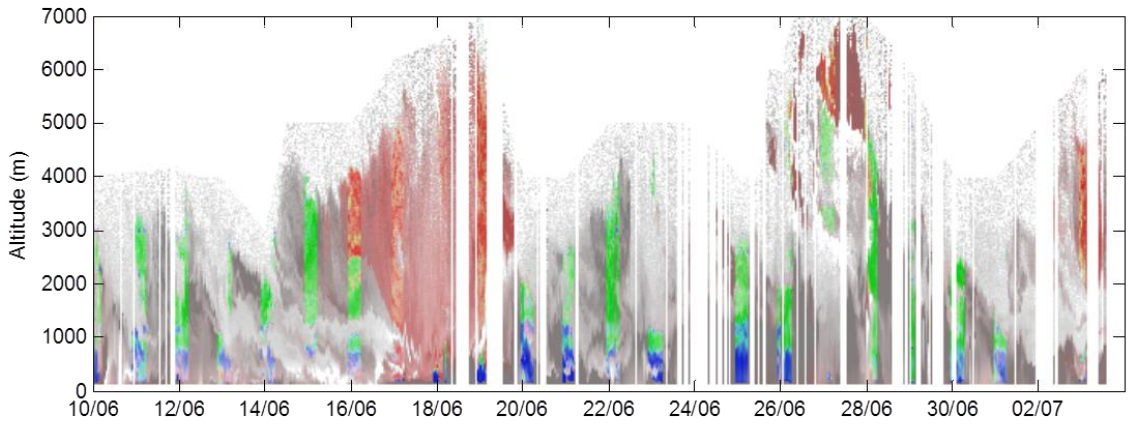

b)

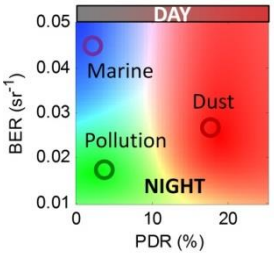

Figure 7: a) Results of aerosol speciation as given by lidar-derived extinction, PDR and BER, with backscatter coefficient coded as saturation (no saturation, white = 0, full saturation = 5 10^{-6} $m^{-1}.sr^{-1}$); b) Key for the colours of the above. Nighttime: dust-, pollution- and marine-like aerosols coded as red, green and blue respectively. Daytime: PDR coded as the saturation of red (top of the colour key). Intermediate colours and grey thus designate undetermined layers where aerosol mixing may occur.

a)

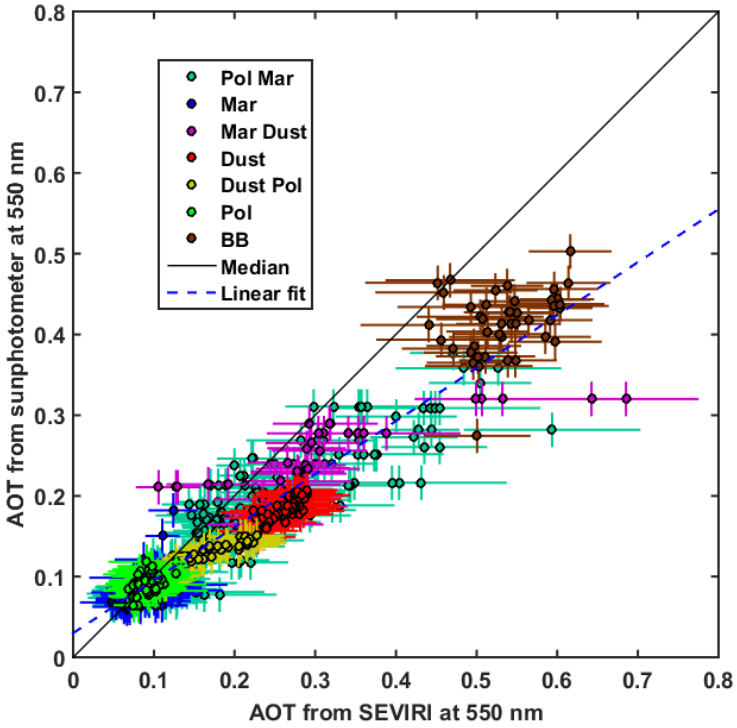

b)

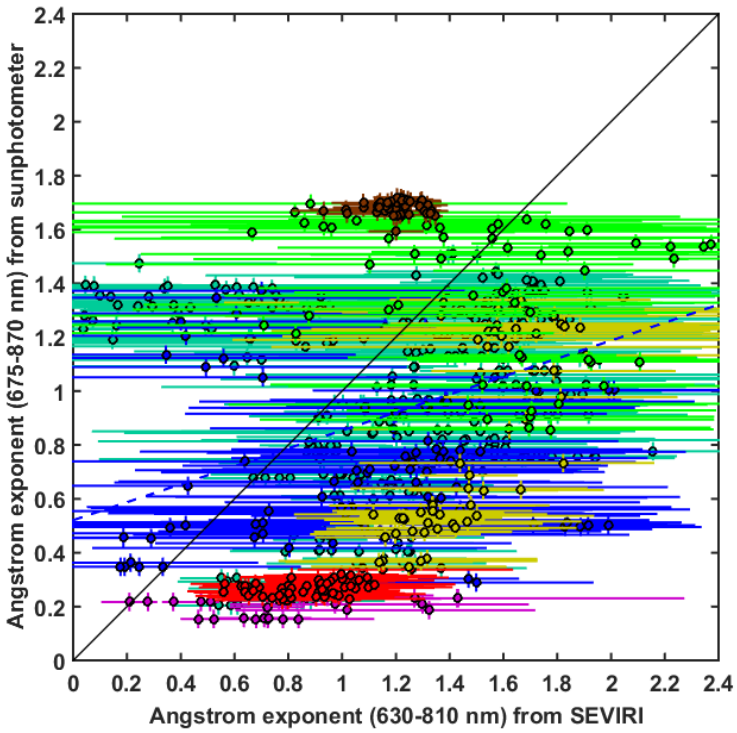

659 Figure 8: a) Scatter plots between SEVIRI and the ground-based sunphotometer of Menorca
660 for the aerosol optical thickness AOT at 550 nm. The dotted line corresponds to the best fit
661 against both retrievals. b) The Ångström exponent for similar spectral ranges. A total of 846
662 coincident data pairs between 10 and 30 June are available for comparison. To the four

aerosol types identified in Figure 7 are added 3 mixed types which are all distinguished by their colour: pollution (Pol), dust (Dust), marine (Mar) and biomass burning (BB), mixing of pollution and marine (Pol Mar), Marine and dust (Mar Dust), dust and pollution (Dust Pol). The solid curve represents the centroid of the distribution.

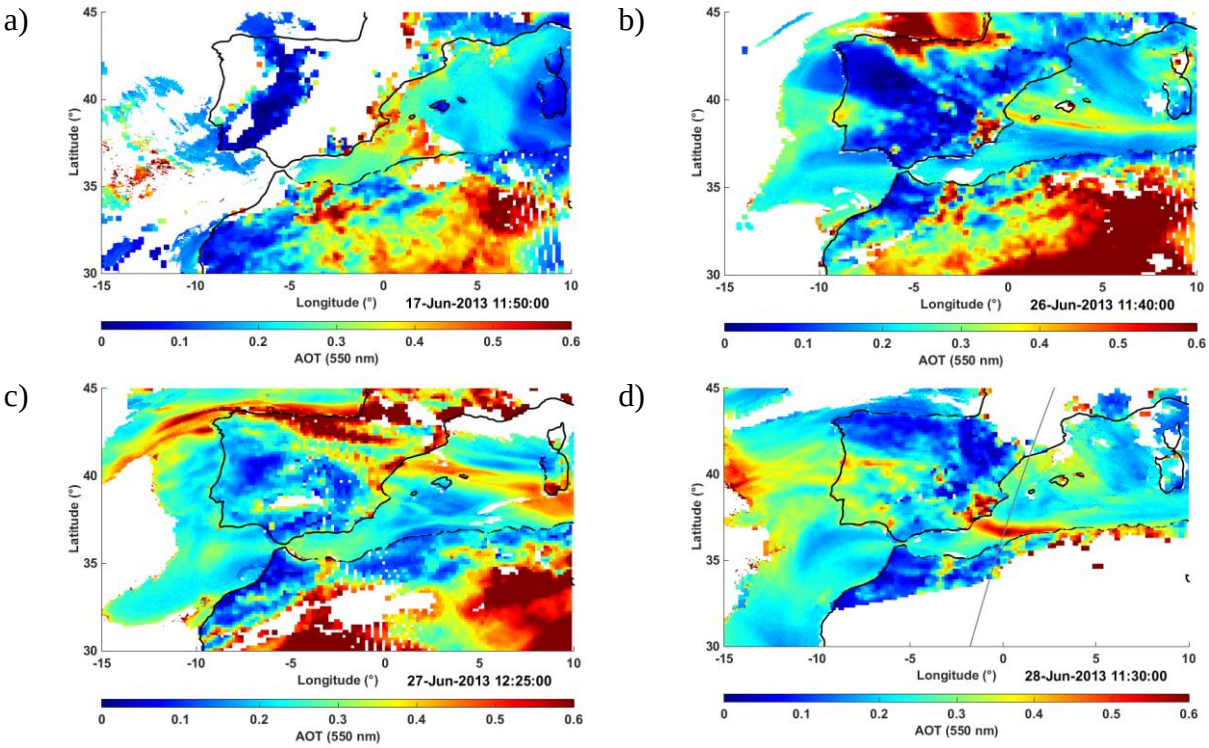

667 Figure 9: AOT composition between the MODIS observations over land and SEVIRI over
668 sea. The SEVIRI AOT was corrected by a factor 0.65 as identified from comparisons with the
669 sunphotometer reported in Figure 8. Top-left panel (a) is for 17 June, top-right (b) for 26 June,
670 bottom-left (c) for 27 June, and bottom-right (d) for 28 June. For 28 June the nighttime
671 CALIOP ground track (at about 2 UTC) is marked by a continuous grey line.

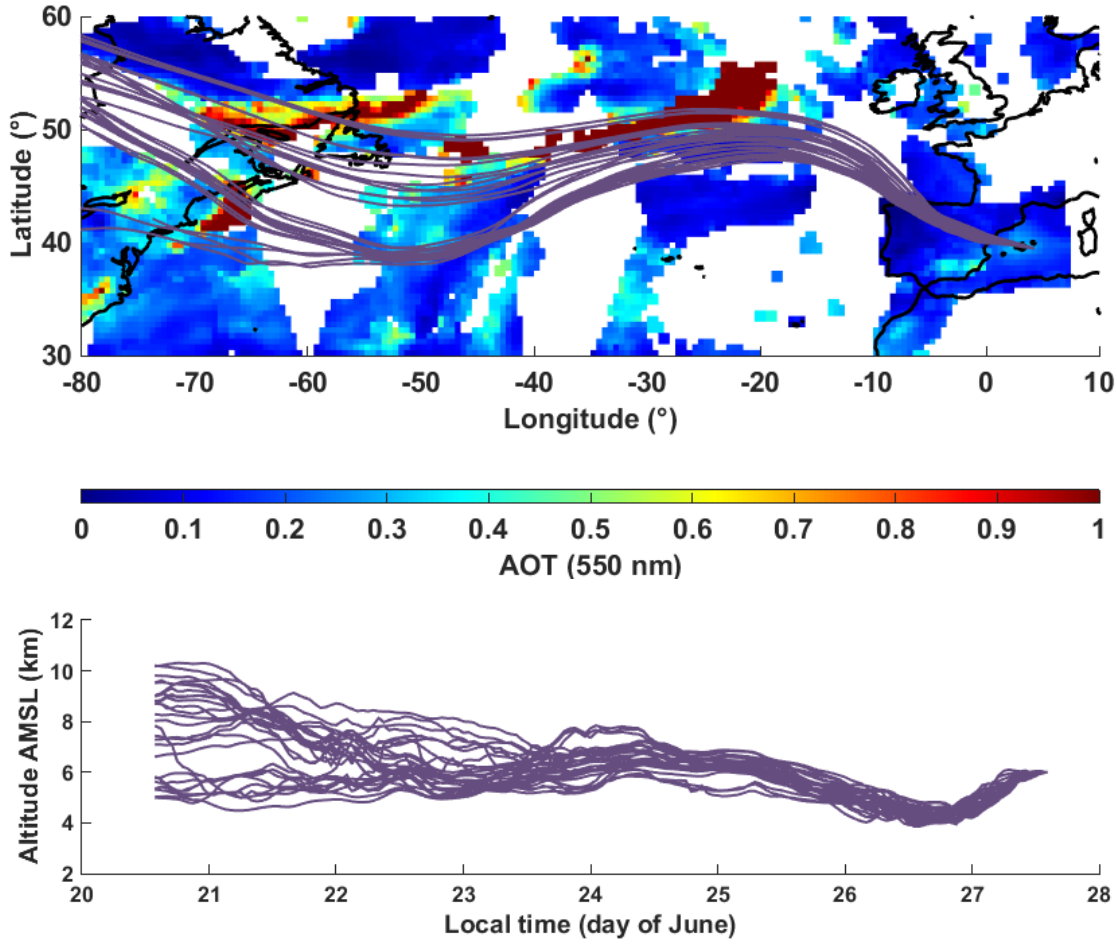

Figure 10: 27 back trajectories from Menorca (39°51′44″N, 4°15′30″E). The back trajectories have been computed using the ensemble mode of the HYSPLIT model (courtesy of NOAA Air Resources Laboratory; http://www.arl.noaa.gov). The end location of the air mass trajectories is at 6 km amsl in the plume detected by the WALI lidar on 27 June, 2013 over Menorca (see Figure 6a). The top panel presents the location of each back trajectory superimposed over the MODIS-derived AOT at 550 nm of 24 June, 2013, for several orbits. The bottom panel shows the altitude of the back trajectories against time.